Evaluating Generic Auto-ML Tools for Computational Pathology

Lars Ole Schwen[a,*], Daniela Schacherer[a], Christian Geißler[b], André Homeyer[a]

[a]*Fraunhofer Institute for Digital Medicine MEVIS, Max-von-Laue-Str. 2, 28359 Bremen, Germany*
[b]*DAI-Labor, Technische Universität Berlin, Ernst-Reuter-Platz 7, 10587 Berlin, Germany*

Abstract

Image analysis tasks in computational pathology are commonly solved using convolutional neural networks (CNNs). The selection of a suitable CNN architecture and hyperparameters is usually done through exploratory iterative optimization, which is computationally expensive and requires substantial manual work. The goal of this article is to evaluate how generic tools for neural network architecture search and hyperparameter optimization perform for common use cases in computational pathology. For this purpose, we evaluated one on-premises and one cloud-based tool for three different classification tasks for histological images: tissue classification, mutation prediction, and grading.

We found that the default CNN architectures and parameterizations of the evaluated AutoML tools already yielded classification performance on par with the original publications. Hyperparameter optimization for these tasks did not substantially improve performance, despite the additional computational effort. However, performance varied substantially between classifiers obtained from individual AutoML runs due to non-deterministic effects.

Generic CNN architectures and AutoML tools could thus be a viable alternative to manually optimizing CNN architectures and parametrizations. This would allow developers of software solutions for computational pathology to focus efforts on harder-to-automate tasks such as data curation.

Keywords: computational pathology, convolutional neural networks, AutoML, hyperparameter optimization, reproducibility

1. Introduction

1.1. Motivation

Automated analysis of digital tissue images holds great potential for improving pathology diagnostics. In addition to increasing the efficiency and reproducibility of disease assessment, it also enables the extraction of novel digital biomarkers for predicting outcomes and treatment response [1, 2]. Image analysis tasks in computational pathology are typically solved using Convolutional Neural Networks (CNNs) [3, 4, 5, 6, 7, 8]. Developing such CNN-based

*Corresponding author
Email address: ole.schwen@mevis.fraunhofer.de (Lars Ole Schwen)

solutions [7] requires multiple steps including data curation and the translation between the diagnostic task and the bare machine learning task.

An essential task in developing a CNN-based solution is the choice of a suitable neural network architecture, its initialization, and (training) hyperparameters [9, 10, 11, 12]. CNN architectures and hyperparameters are usually selected based on experience and manual optimization, where different architectures are tried, multiple trainings are performed, and hyperparameters are adjusted. This process is very time consuming and computationally intensive for a number of reasons: The optimization task is multi-dimensional, involving categorical (e.g., CNN architecture), Boolean (e.g., whether to use certain CNN building blocks), integer (e.g., number of epochs or early stopping patience), and continuous (e.g., learning rate) variables. Evaluating the objective function involves computing a metric after training and evaluating a CNN. This is computationally very expensive, single evaluations may take hours to days to compute. The objective function is neither convex nor is a gradient (approximation) available. Moreover, the objective function is noisy due to non-determinism in CNN training [13, 14, 15].

1.2. State of the art

For some time, research has been carried out on methods to automate the search for optimal CNN architectures and hyperparameters and make these steps more efficient. Such "AutoML" methods have been published for generic applications [16, 17] and medical image analysis [9]. Their main building blocks are automatic neural architecture search [18, 19, 20] and algorithmic hyperparameter optimization [10, 10].

A number of cloud-based generic commercial AutoML tools is available, e.g., Amazon Sage Maker [21], Clarifai [22], Google AutoML Vision [23, 24] and Vertex AI [25], H2.ai [26] MedicMind [27], as well as Microsoft Azure Custom Vision [28]. Besides offering cloud deployment for inference, limited possibilities to download trained classifiers for on-premises use exist as well. Moreover, there is Apple Create ML [29] for offline application of AutoML. These tools are designed as easy-to-use tools for machine learning tasks, in particular image classification, without substantial user configuration [30] or the need for coding experience [31]. Instead, usage requires providing image data and tables with reference results, CNN training is subsequently started via graphical (web) interfaces. While mostly evaluated on standard benchmark tasks like ImageNet or CIFAR-10/-100 (e.g., [32]), cloud-based generic AutoML tools have also been evaluated in medical image analysis [33, 34, 35, 36, 37, 38] and specifically in computational pathology [39, 40, 41].

There are also Auto ML tools for pure on-premises use, such as AutoGluon [42, 43, 44], AutoKeras [45, 46, 47], Auto-PyTorch [48, 49], and model_search [50]. These open-source tools are used as part of code (e.g., Python) and are typically more flexible, requiring more user configuration than the cloud-based tools. Besides generic tools, specialized CNN training tools for biological microscopy image segmentation [51] and histopathology image analysis [52] have been published.

1.3. Contribution

In this article, we evaluate how generic AutoML tools for image classification can be applied to selected use cases in computational pathology. Moreover, we investigate how the resulting classifiers perform compared to reference results from literature for the selected tasks.

2. Methods

2.1. AutoML tools

We evaluated the performance of two generic AutoML tools (AutoGluon version 0.1.0 [53] and AutoML Vision [23] as available between Sep 02 and Sep 22, 2021) for image classification when applied to three different use cases [54, 55, 56] in computational pathology. By "performance," we refer to the "correctness" of the classification results evaluated in task-specific metrics. The evaluated tools were chosen to include one cloud-based and one on-premises tool, both allowing on-premises inference using the trained CNNs. The latter is important if the classifier shall be applied to confidential data, to avoid vendor lock-in by cloud providers, and to allow for a defined hardware plus software setup to ensure reliability, e.g., as required for regulatory approval if the CNN becomes part of a medical product. With AutoGluon originally developed by Amazon [43, 57] and AutoML Vision developed by Google, these tools come from two different major platform providers.

2.2. Example use cases

To evaluate these AutoML tools, we chose the following three use cases covering different types of diagnostic tasks in computational pathology. All three are based on frequently cited publications, so that reference values for the performance assessment were available. Moreover, we required that the underlying datasets were publicly available. All three use cases translate to image classification, the most common application of machine learning in computational pathology.

2.2.1. Tissue classification: lung cancer

From [54], we selected two binary and one ternary classification task, distinguishing normal vs. tumor tissue, lung adenocarcinoma (LUAD) vs. lung squamous cell carcinoma (LUSC) tissue, and normal vs. LUAD vs. LUSC tissue. The authors split data obtained from The Cancer Genome Atlas (TCGA) [58] in training, validation, and test data at the slide level, divided the whole-slide images in image tiles, and trained separate Inceptionv3 CNNs [59] for each image classification task. In these datasets, one class was assigned to all tiles of the entire slide, even if the slide also contained some parts of healthy tissue. The authors evaluated classifier performance at the slide level, averaging prediction probabilities over all tiles belonging to a slide, via the area under the receiver operating curve (AUROC), resulting in 0.993 (for the binary classification normal vs. tumor), 0.950 (LUAD vs. LUSC), 0.984/0.969/0.966 (three-class normal vs. rest/LUAD vs. rest/LUSC vs. rest). The code for [54] is available from [60].

2.2.2. Mutation prediction: microsatellite instability

From [55], we selected the binary classification task of predicting microsatellite instability (MSI) vs. microsatellite stability (MSS) from tissue samples. The authors applied this to three different dataset: tiled whole-slide images of formalin-fixed paraffin-embedded tissue samples of colorectal cancer (CRC-DX), snap-frozen samples of colorectal cancer (CRC-KR), and formalin-fixed paraffin-embedded tissue samples of gastric (stomach) adenocarcinoma (STAD). The data obtained from TCGA was first split at the patient level in two datasets, one for training and validation to be split further, and one for testing. The tile images split in this way are available from [61] (CRD-DX, STAD) and [62] (CRC-KR). Next, training and validation data were split at the tile level 85%:12.5%, the remaining 2.5% of the tiles remained unused [63], in order to train separate ResNet18 CNNs [64] for classifying each dataset. Like in the tissue classification task [54], the authors of [55] evaluated the classifier performance per slide (after averaging prediction probabilities over all tiles for a given slide) in terms of AUROC, resulting in 0.84 (for the CRC-DX dataset), 0.77 (CRC-KR), and 0.81 (STAD).

2.2.3. Grading: Gleason grading from tissue microarrays

From [56], we selected the quaternary classification task of distinguishing Gleason grades 0, 3, 4, and 5 from tissue microarray (TMA) images of prostate biopsies. The authors split the dataset [65] into training, validation, and test data at the TMA level. Regions with different Gleason grades were annotated in each TMA spot by one pathologist; an additional pathologist annotated the test data.

This evaluation differs from the other two use cases: One TMA spot may have regions with different Gleason grades, so only an evaluation at the image tile level makes sense. For this purpose, the authors divided the TMA spots in image tiles of 750^2 pixels and either assigned the single grade annotated for the center 250^2 pixels or discarded the tile in case of non-unique annotation for the center. Moreover, the authors used quadratically weighted Cohen's κ as a classifier performance metric, reflecting that consecutive grades permit a more fine-grained evaluation than categorical classes.

The authors trained a MobileNet CNN [66] and obtained κ values of 0.55 (compared to pathologist 1 who also annotated the training and validation data) and 0.49 (compared to pathologist 2). Note that these values cannot be compared quantitatively to the AUROC values for the other two use cases, but can be compared to the inter-pathologist agreement of 0.66. Subsequently, the authors of [56] used a sliding-window approach to obtain a pixel-wise classification, computed a Gleason score per TMA spot and obtained κ values of 0.75 (algorithm vs. pathologist 1) and 0.72 (algorithm vs. pathologist 2), comparable to an inter-observer agreement of 0.75 (pathologist 1 vs. 2). However, we decided to omit this aggregation step in the evaluation here in order to have one use-case focused on the plain tile classification.

For the present study, this use case also illustrates how data augmentation [67] can be implemented as a preprocessing step before using the evaluated AutoML tools.

2.3. Data preparation

2.3.1. Tissue classification

For the tissue classification use case, we obtained whole-slide images (WSI) at 20× objective magnification from the Genomic Data Commons [68] as specified in the corresponding download manifest [60]. We did not encounter readability issues as mentioned in [54] and used all 2167 downloaded slides. A corresponding metadata file was also available which specified the tissue type (normal, LUAD, LUSC) for each WSI. For each slide, we generated 512^2 px tiles, omitting tiles that show > 50% background as described in [60]: A pixel is considered background if its 8-bit RGB values satisfy $0.299R+0.587G+0.114B > 220$. For reducing computational effort, we subsequently downsampled the tiles to 128^2 px using PIL Image.resize() [69], saving them as JPEG images at quality 75. Preliminary empirical experiments indicated that this way of using the same field of view with fewer image details led to comparable classification quality. The dataset was split at the patient level with the target of training, validation, and test set comprising 70%, 15%, and 15% of the tiles, respectively. We ensured that all tiles from a particular patient are assigned to only one set. This split was thus at a higher level than the slide-level split in [54], making the task slightly harder. For a detailed list of the numbers of patients, slides, and image tiles in this dataset, we refer to Table B.3 in the appendix. This tile preparation and dataset split were run once as a preprocessing step.

2.3.2. Mutation prediction

For the mutation prediction use case, we downloaded the datasets from [61, 62]. The test sets are fixed as separate archives, with file names indicating a split at the patient level. To divide into training and validation data, we split the non-test data at the tile level according to the percentages described in [55]: 85% training and 12.5% validation, with 2.5% of the tiles remaining unused. The second split was done separately per AutoML run, so different trainings used different splits in training, validation, and unused data. For the numbers of patients, slides, and image tiles in this dataset, we refer to Table B.4 in the appendix.

2.3.3. Grading

For the grading use case, we downloaded the dataset from [65] and pre-processed the images as described in [56]. For this purpose, we technically adapted the preprocessing script from [70] and downsampled the images using the ImageMagick [71] convert command line tool. After resampling all images from 750^2 to 250^2 pixels, validation and test tiles were cropped to the center 224^2 pixels.

We used this use case as an example for how data augmentation and balancing needs to be implemented as a preprocessing step before using the AutoML tools. For data augmentation, we cropped 224^2 pixel images at random position in the 250^2 images, randomly applied or omitted horizontal mirroring, vertical mirroring, and 90-degrees rotation (all implemented as numpy array [72] operations), as well as color augmentation in the hue–saturation–value (HSV) color space (which is a realistic variation for histological images and recommended by [67]; implemented using the albumentations Python package [73, 74] with maximal shifts of 20, 30, and 20 for H, S, and V, respectively).

We combined 8-fold data augmentation with oversampling the minority classes. For the numbers of image tiles in this dataset, we refer to Table B.5 in the appendix. For implementational convenience, these steps of tile preparation were run as a preprocessing prior to each AutoGluon run and not just once. By seeding the pseudo-random number generator used for cropping and augmentation, however, we ensured that all trainings were run on the same tile data.

2.3.4. Use with AutoGluon

Datasets in AutoGluon were loaded by specifying a folder with subfolders for each class containing the image tiles. Loading all image tiles at once turned out to be impossible with 32 GiB of RAM. Hence, we randomly split each full dataset in 40 subsets (folders) during preparation, loaded these subsets successively as datasets for use with AutoGluon, and concatenated them to a single dataset.

2.3.5. Use with AutoML Vision

For using datasets with AutoML Vision, image tiles needed to be available in a Google Storage Bucket with a list describing the split in training, validation, and test data as well as the reference classes (in csv, comma-separated values, format). We hence created these csv lists and uploaded them together with the individual image tiles.

The size of a dataset for each cloud AutoML task was limited to one million images. For the mutation prediction and grading use cases, this limit was not reached; we used the same training, validation, and test sets as for AutoGluon. Adaptations were necessary for the tissue classification use case: training and validation data for the "LUAD vs. LUSC" task contained less than one million tiles, so we only reduced the number of test images by random sampling from the original test set. This does not change the task, as we do not use the tile-based performance reported by the cloud tool, but evaluate the actual performance metric on premises as a postprocessing step using the full test set. The "normal vs. tumor" and "normal vs. LUAD vs. LUSC" tasks had more than one million training and validation tiles, so we randomly sampled 820850, 179050, and 100 tiles from the original training, validation, and test sets, respectively. These numbers were chosen such that the relevant sets, training and validation, were kept large and size proportionality between them was preserved. This way, the task became harder, as less training data was used.

2.4. Generating convolutional neural networks

2.4.1. On-premises training using AutoGluon

Based on the available presets for AutoGluon, we evaluated different presets for different CNN architectures with limited time budget for training (up to 6 hours wall-clock time), in order to get a first overview of the performance of the resulting classifiers for all use cases. We then selected the generally most promising preset for a limited hyperparameter optimization (with a time budget for training of 14 days) for one task per use case (LUAD vs. LUSC for the tissue classification, the STAD dataset for the mutation prediction, and the single Gleason grading task)

Table 1: Presets used for the evaluation of AutoGluon (ESP: Early stopping patience, HPO: algorithm for hyperparameter optimization, Budget: training time limit in wall-clock time in hours, BayesOpt: Bayesian optimization as implemented in AutoGluon)

Name	Architecture	Learning rate	Batch size	# Epochs	ESP	HPO	Budget
0	ResNet50_v1b	0.01	64	50	5	none	1
1	MobileNetv3_small	{0.01, 0.005, 0.001}	{64, 128}	{50, 100}	10	BayesOpt, 12 trials	6
2	ResNet18_v1b	{0.01, 0.005, 0.001}	{64, 128}	{50, 100}	10	BayesOpt, 12 trials	6
3	ResNet34_v1b	$[0.0001, 0.01]_{\text{logarithmic}}$	{8, 16, 32, 64, 128}	150	20	BayesOpt, 16 trials	6
4	ResNet50_v1b	0.01	64	50	5	none	6
5	ResNet101_v1d	$[0.00001, 0.01]_{\text{logarithmic}}$	{32, 64, 128}	200	50	BayesOpt, 16 trials	6
HPO	ResNet18_v1b	$[0.0001, 0.01]_{\text{logarithmic}}$	{64, 128}	{50, 100}	10	BayesOpt, 16 trials	336 (14 days)

Table 2: Presets used for the evaluation of AutoML Vision

Preset name (used here)	Name (during setup)	Name (after training)	Training time limit in node hours
A	Best Tradeoff	Mobile Best Tradeoff	2
B	Best Tradeoff	Mobile Best Tradeoff	14 (mutation prediction and grading use cases) 16 (tissue classification use case)
C	Faster Predictions	Mobile Low Latency	14 (mutation prediction and grading use cases) 16 (tissue classification use case)
D	Higher Accuracy	Mobile High Accuracy	16 (mutation prediction and grading use cases) 18 (tissue classification use case)

in order to limit the computational workload. The presets used in this evaluation are listed in Table 1, where the budgets refer to the actual training and exclude preparation steps (e.g., loading datasets) and postprocessing steps (e.g., applying the classifier to the test set). We stored the console output from the training for later analysis and saved the resulting CNN for later evaluation.

2.4.2. Cloud-based training using AutoML Vision

AutoML Vision provided three presets for training CNNs which can be downloaded for offline use. Depending on the dataset size, a training time budget was recommended for the chosen preset. In addition to the recommended budgets for the three presets, we also used the default preset with a training budget limited to 2 node-hours. These presets are listed in Table 2. Further configuration of the training was neither needed nor possible.

2.5. Tile-based inference

2.5.1. On-premises inference using AutoGluon

AutoGluon permitted loading the classifier trained in the previous step and loading datasets for inference in the same way as for training. The trained classifier was applied and the resulting predicted classes/prediction probabilities for the individual image file names were saved as csv lists. This worked in the same way for all three use cases,

using the previously prepared datasets. We ran the inference separately for all training, validation, and test datasets, storing the respective csv files for later evaluation.

2.5.2. On-premises inference using AutoML Vision

AutoML Vision permitted exporting the trained models to TensorFlow Lite format (among other formats) for offline use. This resulted in an integer-quantized CNN which could be downloaded from an associated Google storage bucket. We loaded these CNNs in a Python program to run the inference, this time on the test data only. With custom Python code, we saved predictions and prediction probabilities in the same csv format as produced by AutoGluon.

2.6. Evaluation of classifier performance

The tile-based results of the classifiers created with both AutoML tools were used as the basis for calculating the specific performance metrics for each use case.

The tissue classification and mutation prediction use cases used the same evaluation metric, i.e., slide-based AUROC [54, 55]. This involved aggregating tile-based classification results to a slide-based result by arithmetically averaging class-wise prediction probabilities, where the tile-to-class mapping was available from the TCGA file names. Then, we compute AUROCs from the slide-based class prediction probabilities using the Python module Scikit-learn [75, 76]. For the ternary classification task, each class was separately compared to the combination of the other two classes, i.e., we computed multiclass one-vs-rest ROCs.

For the grading use case, quadratically weighted Cohen's κ was used as the performance metric. We computed these values using the Python module Scikit-learn [75, 76], comparing the output of the classifiers separately to the classifications of the two pathologists who annotated the test data.

2.7. Implementation and hardware

For the evaluation of AutoGluon, the entire processing pipeline was implemented as custom shell and Python scripts and executed in a Docker [77] container using one GPU (NVIDIA GeForce GTX 1080 Ti or RTX 2080 Ti with 11178 or 11019 MiB GPU RAM).

For use with AutoML Vision, each of the preprocessed datasets was exported from the preprocessing as part of the AutoGluon pipeline. The on-premises inference using the downloaded classifiers from AutoML Vision was implemented using Python code, the respective metrics were evaluated using the same code as above. These scripts were executed in a Docker container running locally on a PC with one NVIDIA GeForce GTX 1080 GPU with 8117 MiB GPU RAM.

2.8. Evaluation of hyperparameter optimization

For evaluating the effect of the hyperparameter optimization (HPO), we analyzed the AutoGluon console outputs for the preset HPO. AutoGluon printed status information during its trials, but only saved what it found as the best classifier at the end. Hence, classifier performance could only be assessed on a tile level for the training and

validation data, but neither for the test data nor via slide-based performance metrics. From the console output, we parsed the values of the hyperparameters being optimized, the processing speed (images per second; per batch and per epoch), the training accuracy (per batch and per epoch), and the validation accuracy (per epoch and at the end of each trial, after potential early stopping).

2.9. Evaluation of reproducibility

Since training and evaluation of CNN-based classifiers are not fully deterministic processes [13, 14, 15, 78, 79], it is important to examine whether differences in the performance of classifiers are meaningful or merely random effects. For assessing the impact of these effects on classifier performance, we repeated the entire AutoML run and evaluation for selected presets six times in addition to the initial run for the same tasks selected for hyperparameter optimization. In these repetitions, we refrained from reducing variability for those effects we could have controlled (e.g., seeding pseudo-random number generators or avoiding concurrent system load) in order to have a scenario better resembling the attempt to reproduce literature results. Given the relatively small number of samples and, in particular, just a single reference value per reproducibility experiment, we omitted a potentially misleading assessment of statistical significance.

3. Results

3.1. Usage of the AutoML tools

AutoGluon was relatively easy to set up for usage in Docker: a current nvidia/cuda image needed only a few additional system and python packages. AutoGluon starts the training of a CNN of the specified architecture pre-trained on ImageNet [80] and saves the trained CNN in a custom format of Gluon for later use. The presets with budgets of 1h and 6h did not complete the planned number of trials in the respective time budget, the hyperparameter optimization presets with a budget of 14 days finished all 16 trials within 11d 12:17h for the tissue classification use case, 1d 17:11h for the mutation prediction use case, and 1d 16:06h for the grading use case (sic: tissue classification took ten days longer than the other two use cases).

AutoML Vision did not provide any log of the initialization, potential network architecture search, or hyperparameter optimization. The platform allowed downloading the trained CNN in TensorFlow Lite format (among other formats). The resulting networks appeared to be variants of MnasNet [81], with the same overall structure. The number of channels (and thus number of network parameters) differed throughout the building blocks of the CNN depending on the preset and, in the final layers, depending on the number of classes. The network outputs 8-bit (unsigned integer) quantized class probabilities. The AutoML runs using presets B to D (see Table 2) typically took less than half the specified time budget, i.e., finished within a similar time as the budget used for AutoGluon.

The dockerized code for preprocessing data, running AutoGluon to generate CNNs (AutoGluon only), and evaluating the resulting classifiers (AutoGluon and AutoML Vision) is available from [82].

3.2. Performance of classifiers obtained from presets

3.2.1. AutoGluon

In the initial evaluation of AutoGluon, preset 2 generally generated the best-performing classifiers, see Figure 1 (large blue crosses).

For the tissue classification use case, distinguishing normal from tumor tissue (two-class normal vs. tumor, three-class normal vs. other) seems to be a comparably easy task, since AUROCs were generally larger than 0.99. The AutoGluon-trained classifiers produced AUROCs even closer to 1 than the reference results from the literature. For the distinction between LUAD and LUSC (two-class task) as well as for the LUAD vs. other and LUSC vs. other (three-class task), the performance of the AutoGluon-generated classifiers was almost on par with the literature results.

For the mutation prediction use case, the AutoGluon-generated classifiers resulted in slightly higher AUROCs for two of the datasets and a slightly lower AUROC for the third dataset.

For the grading use case, κ values compared to pathologist 1 were slightly higher and κ values compared to pathologist 2 were slightly lower than the literature reference for the AutoGluon-generated classifiers. As pathologist 1 created the annotations for the training and validation data, this may indicate a slightly stronger overfitting of the algorithm to this observer than the literature result, possibly due to our oversampling.

Given the relatively high variability when repeating the AutoML runs (cf. below), we refrained from computing potentially misleading improvement percentages in the comparisons throughout this section.

3.2.2. AutoML Vision

The classifiers generated by AutoML Vision generally performed similarly to those generated by AutoGluon and the reference results, see Figure 1 (large red crosses). Unlike the AutoGluon-generated classifiers that output floating-point numbers, the classifiers generated by AutoML Vision output 8-bit integer-quantized prediction probabilities. The resulting small number of possible values causes many ties when finding the class with highest probability. These ties were resolved in the evaluation by using the "first" class with maximum probability, where "first" refers to an order opaquely chosen by AutoML Vision (constant per dataset in our observations).

Among the presets, none was generally superior to the others, in particular not the one named "higher accuracy." This observation also held for the tile-based average accuracy reported after training, even in those cases where the full test data was available for cloud evaluation. Presets A and D failed to generate a meaningful classifier in one case each, these classifiers predicted the same class for all test tiles. For the "normal vs. tumor" task, this happened after reaching the budget limit of 2 node-hours, and the classifier constantly predicted one class with high probability (244/256). For the "LUAD vs. LUSC" task, the AutoML run stopped prior to reaching the budget limit (after 5.957 of 16 node-hours) for unknown reasons. In this case, the classifier predicted both classes with a probability of 0.5 for all tiles. For the tissue classification use case, the classifiers generated by AutoML Vision resulted in AUROCs even closer to 1 than the AutoGluon-generated classifiers for the tasks distinguishing normal and tumor slides (two-class

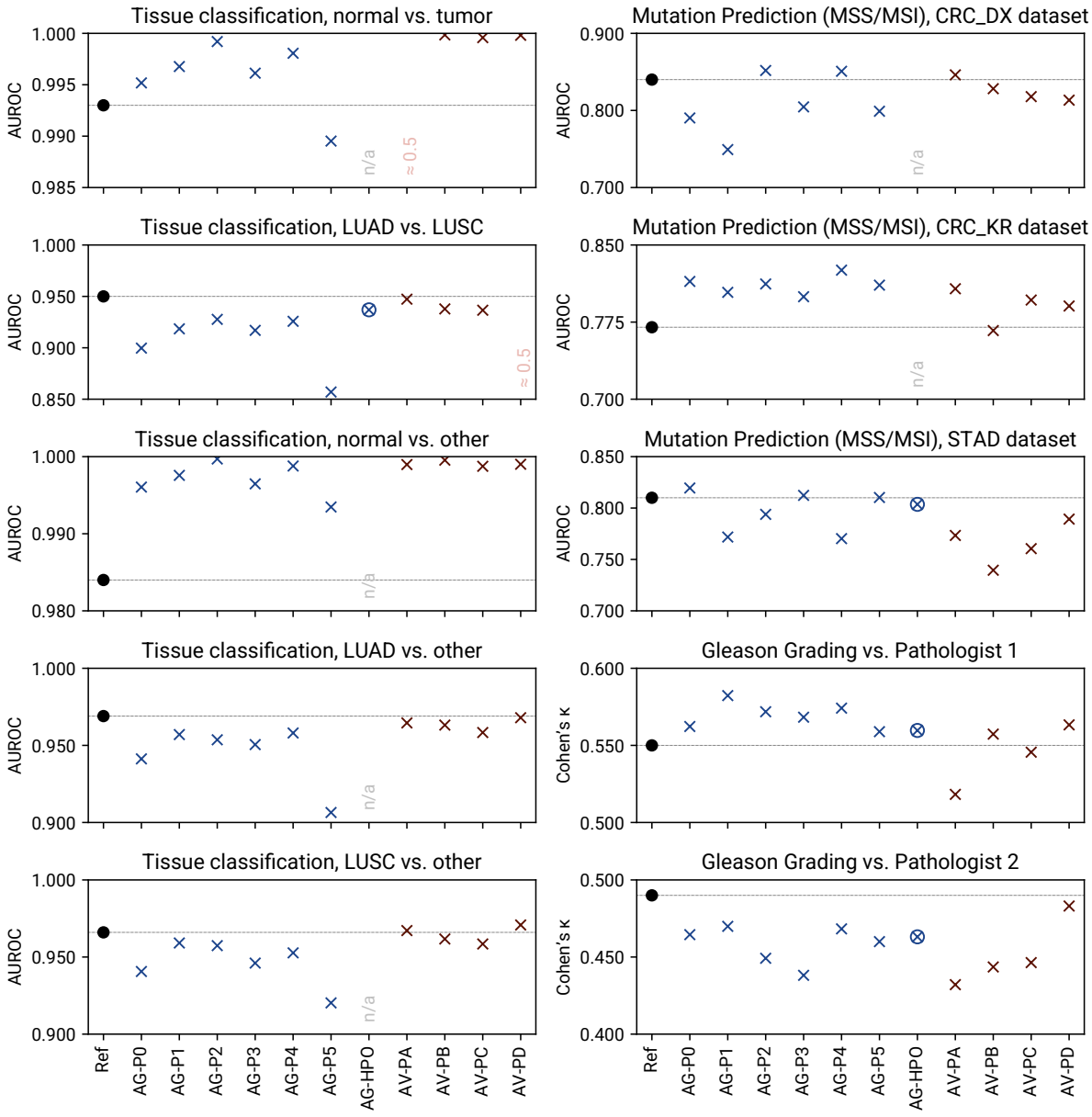

Figure 1: Overview of classifier performance. Classifier performance is quantified in the respective metrics for the tasks of our use cases, results for the AutoGluon (AG; blue crosses) and AutoML Vision (AV; red crosses) are compared to the reference results from literature (black circles). For AutoGluon, the circled cross indicates the results of the preset completing a limited hyperparameter optimization. ("n/a" indicates those tasks where the HPO preset was not run; "≈ 0.5" indicates classifiers returning constant classes, i.e., where the AutoML optimization clearly failed).

normal vs. tumor, three-class normal vs. other). For the two-class LUAD and LUSC task as well as for the three-class LUAD vs. other and LUSC vs. other tasks, AUROCs were slightly higher than for the AutoGluon-generated classifiers and in the same range as the reference results. For the mutation prediction use case, AUROCs are in the same range as the literature results and as for the AutoGluon-generated classifiers. For the grading use case, κ values were slightly lower than for the AutoGluon-generated classifiers, and in the same range as the reference results.

3.3. Impact of hyperparameter optimization

Our hyperparameter optimization in AutoGluon led to slightly, but not substantially better classifier performance compared to preset 2 for the tissue classification and mutation prediction use cases, see Figure 1. For the grading use case, the classifier performance was slightly better than the one for preset 2 for pathologist 2's annotations, but interestingly slightly worse for pathologist 1's annotations.

4. Hyperparameter optimization

A more detailed analysis of the tile-based accuracies (Appendix C) corroborated this observation: for the tissue classification and grading use cases (Figures C.3 and C.5), validation did not substantially improve compared to the initial trial. While there was a substantial improvement for the mutation prediction use case (Figure C.4); this was actually due to the initial parametrization being different from the one in preset 2. Among the hyperparameters optimized, learning rate had the highest influence on classifier performance. Generally, a larger learning rate led to better classifier performance, so it might have made sense to extend the search range beyond 10^{-2}.

AutoGluon presets 1, 2, 3, and 5 also included partial hyperparameter optimization to the extent possible within the time budget of 6 hours. In 18 of the 60 cases, more than one trial was started. In 4 of those 18 cases, accuracy increased after the first trial, but none of these improvements was substantial.

AutoML Vision did not report whether or not hyperparameter optimization took place during the respective run.

4.1. Reproducibility

The reproducibility analysis for selected tasks (see Figure 2) showed notable variability of the performance metrics, including cases where the first AutoML run yielded worse results than the six repetitions for some of the tasks.

The classifiers generated by AutoML Vision were more variable than the AutoGluon-generated ones. This variance included one particularly obvious outlier in the comparison to both pathologists, resulting from the same repetition. Given the small number of repetitions in this study and the single reported reference results, we refrained from a potentially misleading statistical significance analysis.

The variability was particularly large for the grading use case. This was probably because the tile-based results were not aggregated per slide, so there was no compensation for misclassifications. In fact, a more detailed analysis

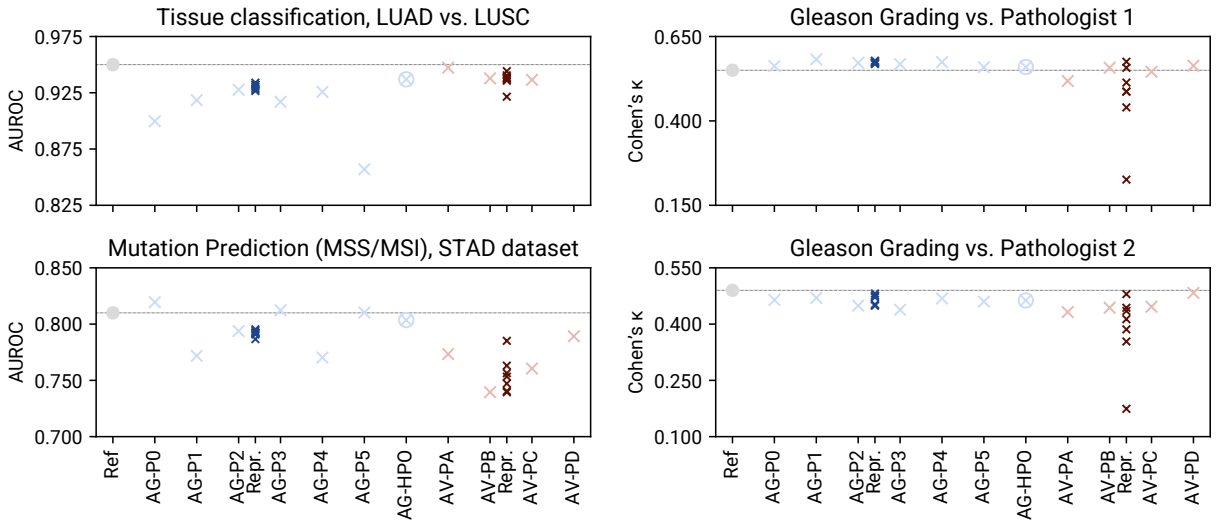

Figure 2: Variability of AutoML results. For selected tasks, classifier performances are shown for one AutoGluon (blue) and one AutoML Vision (red) preset for an additional six runs. The bright crosses show the results from the initial run for all presets for comparison.

of the per-tile predictions for the other use cases also showed higher variability than the aggregated results, see Appendix D.

The range of values obtained from these repeated AutoML runs using the same data cannot be directly compared to confidence intervals reported in [54] and [55], which were obtained by bootstrapping the test data for fixed classifiers. We also computed these for completeness, see Appendix E.

5. Discussion

5.1. Comparison of AutoGluon and AutoML Vision

As an open-source tool, AutoGluon allows insight into how it performs the individual runs and permits adaptation if needed. In contrast, AutoML Vision is a black-box tool whose internals may change without users noticing. In both cases, the generated CNNs and their execution environment are under the control of the user, allowing transparent evaluation (e.g., for quality assurance purposes) of the resulting classifiers.

AutoGluon allows setting network architectures and parametrizing the hyperparameter optimization, whereas AutoML Vision only allows selecting one of three presets and a run-time budget, for which a recommendation is given based on the dataset size. This gives AutoGluon more flexibility at the cost of higher usage complexity.

AutoGluon can be used on premises, so confidentiality and privacy of training data can be ensured. In contrast, cloud-based tools like AutoML Vision may be incompatible with local data protection regulations. On-premises tools require appropriate GPU resources and maintenance of the corresponding systems, while cloud-based tools incur costs for cloud data storage, data transfer, and, most importantly, GPU time.

In the AutoML Vision evaluation for the tissue classification use case, we observed two cases where the classifier predicted a constant single class for the entire test set, which suggests an obviously failed training. In contrast, the outlier in the Gleason grading corresponds to a classifier predicting different classes (a small proportion of which agree with the reference results). Just this single result is insufficient to identify the corresponding classifier as sub-optimal.

Both tools allow tile-based inference within the tool itself, i.e., AutoML Vision allows deploying the generated CNNs for inference in the cloud. We decided to run this step on premises in order to be able to better control and review the evaluation. Aggregating CNN output per tile to an assessment per slide is a step not necessarily supported in generic AutoML tools and, thus, needs to be implemented as a postprocessing step in either case.

The performance of the classifiers obtained for the three selected use-cases using the two selected AutoML tools was generally on par with literature results. While the reference results in the literature were obtained with network architectures and training specifically optimized for the respective task, we obtained our classifiers using generic presets with minimal interaction effort.

For AutoGluon, generally our preset 2 seemed to be a good choice to obtain consistently good classifiers, both independent of the specific use case and independent of non-deterministic effects. The limited hyperparameter optimization evaluated here resulted in much larger computational effort (46-fold, 6.9-fold, and 6.7-fold), but no substantial improvement of classifier performance. For AutoML Vision, our results do not permit a clear preset recommendation. However, given that the resulting classifiers can sometimes be useless or sub-optimal, it may be necessary to perform additional AutoML runs.

5.2. Reproducibility

The results of the reproducibility analysis illustrate two rather fundamental effects also occurring independently of AutoML: non-determinism in Deep Learning and the robustness of aggregated metrics.

It is well known that training and evaluation of CNN-based classifiers are not fully deterministic processes [13, 14, 15, 78, 79] due to multiple effects:

- The system used (including but not limited to the GPU) and concurrent load on the system (in particular for disk cache/input/output and CPU) may differ.
- In combination with a run-time budget specified in wall-clock time, actual computational resources may differ.
- Seeding of pseudo-random number generators may differ (for the actual training, but also for pre- and post-processing), explicit seeding may not be available via the AutoML tool.
- Order of data files read from disk may vary, resulting in different training/validation/test splits and training order.
- Parallelization of floating-point arithmetics on the GPU is inherently non-deterministic [83, 84].

These effects mostly have an impact on the training due to its multiple iterations, but may also affect inference. In particular, the non-determinism for training runs with the same hyperparameters poses a problem for hyperparameter optimization by making the objective function noisy, regardless whether algorithmic or manual optimization is used.

Our approach was to run the training under essentially the same conditions from the perspective of a naive user of the AutoML tools. In particular, we did not dig into the source code of AutoGluon to work out where pseudo-random number generators seeding would be needed, and we did not run the AutoML on a system without concurrent jobs. For AutoML Vision, these aspects were beyond our control in the cloud platform in any case. A more detailed investigation of the contributions of individual effects, how they could be mitigated, and how non-determinism interacts with hyperparameter optimization is beyond the scope of the present study. Such an investigation could involve separating training and inference by using single-threaded code on the CPU for inference; seeding pseudo-random number generators to the extent possible; using a system exclusively without concurrent computational jobs; etc.

The larger variability at the tile level (see Appendix D) is actually what characterizes reproducibility of the runs of the AutoML tools; aggregated performance metrics may obfuscate such non-determinism. On the other hand, this discrepancy indicates that the underlying (diagnostic) tasks are robust with respect to misclassifications of part of the data for separate cases. One way to mitigate or profit from this variability is to generate multiple CNNs and use them as an ensemble [85, 86, 87, 88, 89], either at the tile level before aggregating information per slide, or at the slide level—a detailed investigation of which is also beyond the scope of this study.

5.3. Limitations and outlook

Besides the points mentioned above, the biggest limitation of this study is the number of use cases considered and the limitation to tasks addressable by image classification. While we selected three use cases to cover typical tasks in computational pathology, our findings should be confirmed or disproven in more applications, e.g., those listed in [90]. With easy-to-use generic AutoML tools becoming more flexible and with the development of self-configuring approaches for medical image analysis tasks [91, 92], an evaluation of these techniques for tasks in computational pathology also seems within reach.

A second major limitation is that we only evaluated two AutoML tools. While this is sufficient to show that AutoML tools can achieve performance on par with reference results from literature, a comparison with additional available tools would be interesting. This should involve generic on-premises tools (e.g., [45, 48, 50]) generic cloud tools (such as [21, 25, 28]), and tools specific for computational pathology (e.g., [52]). The latter can have the advantage of containing re-usable building blocks needed for histological images independent of the specific diagnostic task, such as tiling of whole-slide images and the per-slide aggregation of inference results [7] and corresponding specialized loss functions or evaluation metrics, as well as targeted image modifications for data augmentation or normalization [67].

Within the AutoGluon experiments, we defined separate presets for separate CNN architectures to have a clearer separation of parameters varied during hyperparameter optimization, making sure all architectures are tried within limited run-time. For a neural architecture search other than trying standard architectures, a different platform would be needed. Moreover, our hyperparameter optimization only ran for 16 trials, using a limited set of parameters with limited ranges in order to evaluate what is achievable within typically available computational resources (about 11.5 days). It would be interesting to extend both neural architecture search and hyperparameter optimization to investigate whether substantially larger computational effort can robustly yield higher performance than the reference results.

Our comparison of classifier performance was based on (differences of) data-driven metrics, AUROC and quadratically weighted Cohen's κ, to allow a numerical comparison. This is purely a data science perspective and needs to be complemented by an assessment by domain experts (pathologists) in a suitable study with classifiers integrated in a practical diagnostic workflow.

Further potential for domain-specific improvement lies in CNN initialization. For image classification, CNNs are typically pre-trained on ImageNet [80] to benefit from transfer learning [93]. For histological images, pre-training on other computational pathology tasks can be beneficial in order to exploit synergies due to specific image characteristics different from photographs of everyday objects as contained in ImageNet. Such approaches include autoencoders [94, 95] or training (parts of) single CNNs for multiple tasks [96], possibly in a federated manner [97, 98, 99].

From a statistical point of view, the obtained performance values need to be interpreted carefully. In order to have a meaningful comparison between different presets, we used a single set of test data per task for all presets. This might overestimate the performance for data beyond the present datasets, a further independent test set would be needed for a proper estimation of how the performance generalizes. Furthermore, we largely followed the dataset splitting strategies of the original publications in order to obtain comparable results. This, however, results in heterogeneous approaches for the three use cases, not always ensuring splits per patient.

The results presented here were obtained using a specific version of AutoGluon fixed at the beginning of the in-silico experiments and the unspecified version of AutoML Vision while our cloud AutoML experiments were run. These results do not necessarily generalize to later versions.

From a more general perspective, AutoML tools as investigated in this study only address one aspect of developing solutions in computational pathology [7]. Both domain and machine learning expertise remain indispensable for properly translating between a diagnostic task with its evaluation metrics and a machine learning task with its associated loss and metrics. While reducing manual efforts for optimizing CNN architectures and training procedures, generic AutoML tools do not obviate the need for domain-specific data curation. Detecting and addressing potential bias and imbalance in the datasets [6, 100, 101] remains essential. Morevoer, to ensure generalization beyond the training data [102], suitable data normalization [6, 103, 104] and augmentation [67, 105, 6] need be employed, also in combination with data balancing strategies [6, 106, 107].

6. Conclusions

The generic AutoML tools AutoGluon and AutoML Vision are capable of generating image classifiers whose performance is on par with literature results for selected use cases in computational pathology. The impact of actual AutoML features is unclear; AutoGluon relied on a generic preset for CNN architecture and training hyperparameters. The AutoML tools thus eliminate the need to manually search for neural architectures and optimize hyperparameters, which can significantly reduce development effort and allow developers to focus on harder-to-automate tasks like data curation.

CRediT authorship contribution statement

Lars Ole Schwen: Conceptualization, Methodology, Software, Data Curation, Writing – Original Draft, Visualization **Daniela Schacherer:** Software, Data Curation, Writing – Review **Christian Geißler:** Writing – Review **André Homeyer:** Conceptualization, Methodology, Writing – Review, Project administration, Funding acquisition

Acknowledgments

The authors would like to thank Rieke Alpers for advice on statistics. This study was funded by the German Federal Ministry for Economic Affairs and Energy (BMWi) via the EMPAIA project, grant numbers 01MK20002B (LOS, DS, AH) and 01MK20002C (CG). The sponsors had no role in the study design; in the collection, analysis and interpretation of data, in the writing of the manuscript; and in the decision to submit the manuscript for publication; nor did the developers or providers of any AutoML tools.

Declaration of Competing Interest

The authors declare that they have no known competing financial interests or personal relationships that could have appeared to influence the work reported in this paper.

References

[1] B. Acs, M. Rantalainen, J. Hartman, Artificial intelligence as the next step towards precision pathology, Journal of Internal Medicine (2020). doi:10.1111/joim.13030.

[2] K. Bera, K. A. Schalper, D. L. Rimm, V. Velcheti, A. Madabhushi, Artificial intelligence in digital pathology—new tools for diagnosis and precision oncology, Nature Reviews Clinical Cncology 16 (11) (2019) 703–715. doi:10.1038/s41571-019-0252-y.

[3] A. V. Parwani, Next generation diagnostic pathology: use of digital pathology and artificial intelligence tools to augment a pathological diagnosis, Diagnostic Pathology 14 (138) (2019) 1–3. doi:10.1186/s13000-019-0921-2.

[4] M. Cui, D. Y. Zhang, Artificial intelligence and computational pathology, Laboratory Investigation 101 (2021) 412–422. doi:10.1038/s41374-020-00514-0.

[5] G. Campanella, M. G. Hanna, L. Geneslaw, A. Miraflor, V. W. K. Silva, K. J. Busam, E. Brogi, V. E. Reuter, D. S. Klimstra, T. J. Fuchs, Clinical-grade computational pathology using weakly supervised deep learning on whole slide images, Nature Medicine 25 (8) (2019) 1301–1309. doi:10.1038/s41591-019-0508-1.

[6] D. Komura, S. Ishikawa, Machine learning approaches for pathologic diagnosis, Virchows Archiv 475 (2) (2019) 131–138. doi:10.1007/s00428-019-02594-w.

[7] A. Janowczyk, A. Madabhushi, Deep learning for digital pathology image analysis: A comprehensive tutorial with selected use cases, Journal of Pathology Informatics 7 (3) (2016). doi:10.4103/2153-3539.186902.

[8] E. Abels, L. Pantanowitz, F. Aeffner, M. D. Zarella, J. van der Laak, M. M. Bui, V. N. P. Vemuri, A. V. Parwani, J. Gibbs, E. Agosto-Arroyo, et al., Computational pathology definitions, best practices, and recommendations for regulatory guidance: a white paper from the digital pathology association, Journal of Pathology 249 (3) (2019) 286–294. doi:10.1002/path.5331.

[9] C. Ritter, T. Wollmann, P. Bernhard, M. Gunkel, D. M. Braun, J.-Y. Lee, J. Meiners, R. Simon, G. Sauter, H. Erfle, et al., Hyperparameter optimization for image analysis: application to prostate tissue images and live cell data of virus-infected cells, International Journal of Computer Assisted Radiology and Surgery 14 (11) (2019) 1847–1857. doi:10.1007/s11548-019-02010-3.

[10] J. Bergstra, B. Komer, C. Eliasmith, D. Yamins, D. D. Cox, Hyperopt: a python library for model selection and hyperparameter optimization, Computational Science & Discovery 8 (1) (2015) 014008. doi:10.1088/1749-4699/8/1/014008.

[11] R. Liaw, E. Liang, R. Nishihara, P. Moritz, J. E. Gonzalez, I. Stoica, Tune: A research platform for distributed model selection and training, arXiv:1807.05118 [cs.LG] (2018).
URL https://arxiv.org/abs/1807.05118

[12] P. Ren, Y. Xiao, X. Chang, P.-Y. Huang, Z. Li, X. Chen, X. Wang, A comprehensive survey of neural architecture search: Challenges and solutions, ACM Computing Surveys 54 (4) (2021) 1–34. doi:10.1145/3447582.

[13] H. V. Pham, S. Qian, J. Wang, T. Lutellier, J. Rosenthal, L. Tan, Y. Yu, N. Nagappan, Problems and opportunities in training deep learning software systems: an analysis of variance, in: Proceedings of the 35th IEEE/ACM International Conference on Automated Software Engineering, 2020, p. 771–783. doi:10.1145/3324884.3416545.

[14] M. Morin, M. Willetts, Non-determinism in tensorflow resnets, arXiv:2001.11396 [cs.LG] (2020).
URL https://arxiv.org/abs/2001.11396

[15] P. Nagarajan, G. Warnell, P. Stone, The impact of nondeterminism on reproducibility in deep reinforcement learning, in: Proceedings of the 2nd Reproducibility in Machine Learning Workshop at ICML 2018, 2018.
URL https://openreview.net/forum?id=S1e-OsZ4e7

[16] R. Elshawi, S. Sakr, Automated machine learning: Techniques and frameworks, in: European Big Data Management and Analytics Summer School, 2019, p. 40–69. doi:10.1007/978-3-030-61627-4_3.

[17] R. Elshawi, M. Maher, S. Sakr, Automated machine learning: State-of-the-art and open challenges, arXiv:1906.02287 [cs.LG] (2019).
URL https://arxiv.org/abs/1906.02287

[18] H. Pham, M. Guan, B. Zoph, Q. Le, J. Dean, Efficient neural architecture search via parameters sharing, in: International Conference on Machine Learning, PMLR, 2018, p. 4095–4104.
URL http://proceedings.mlr.press/v80/pham18a.html

[19] T. Elsken, J. H. Metzen, F. Hutter, Neural architecture search: A survey, The Journal of Machine Learning Research 20 (1) (2019) 1997–2017.
URL https://www.jmlr.org/papers/v20/18-598.html

[20] B. Zoph, V. Vasudevan, J. Shlens, Q. V. Le, Learning transferable architectures for scalable image recognition, in: Proceedings of the IEEE Conference on Computer Vision and Pattern Recognition, 2018, p. 8697–8710. doi:10.1109/CVPR.2018.00907.

[21] Amazon Web Services, Image classification algorithm - Amazon SageMaker (2021).
URL https://docs.aws.amazon.com/sagemaker/latest/dg/image-classification.html

[22] The world's AI | clarifai computer vision & machine learning platform (2021).
URL https://www.clarifai.com/

[23] AutoML Vision documentation (2021).
URL https://cloud.google.com/vision/automl/

[24] E. Bisong, Building machine learning and deep learning models on Google Cloud Platform, APress/Springer, 2019. doi:10.1007/978-1-4842-4470-8.

[25] Vertex AI, Google Cloud (2021).
URL https://cloud.google.com/vertex-ai

[26] AutoML in H2O.ai | H2O.ai (2021).
URL https://www.h2o.ai/products/h2o-automl/

[27] Deep learning - medicmind (2021).
URL https://www.medicmind.tech/

[28] Microsoft, Custom vision (2021).
URL https://www.customvision.ai/

[29] Creating an image classifier model, Apple Developer Documentation (2020).
URL https://developer.apple.com/documentation/createml/creating_an_image_classifier_model

[30] C. O'Byrne, A. Abbas, E. Korot, P. A. Keane, Automated deep learning in ophthalmology: AI that can build AI, Current Opinion in Ophthalmology 32 (5) (2021) 406–412. doi:10.1097/ICU.0000000000000779.

[31] L. Faes, S. K. Wagner, D. J. Fu, X. Liu, E. Korot, J. R. Ledsam, T. Back, R. Chopra, N. Pontikos, C. Kern, et al., Automated deep learning design for medical image classification by health-care professionals with no coding experience: a feasibility study, The Lancet Digital Health 1 (5) (2019) e232–e242. doi:10.1016/S2589-7500(19)30108-6.

[32] X. He, K. Zhao, X. Chu, AutoML: A survey of the state-of-the-art, Knowledge-Based Systems 212 (2021) 106622. doi:10.1016/j.knosys.2020.106622.

[33] A. A. Borkowski, N. A. Viswanadhan, L. B. Thomas, R. D. Guzman, L. A. Deland, S. M. Mastorides, Using artificial intelligence for COVID-19 chest X-ray diagnosis, Federal Practitioner 37 (9) (2020) 398. doi:10.12788/fp.0045.

[34] E. Korot, Z. Guan, D. Ferraz, S. K. Wagner, G. Zhang, X. Liu, L. Faes, N. Pontikos, S. G. Finlayson, H. Khalid, et al., Code-free deep learning for multi-modality medical image classification, Nature Machine Intelligence 3 (4) (2021) 288–298. doi:10.1038/s42256-021-00305-2.

[35] I. K. Kim, K. Lee, J. H. Park, J. Baek, W. K. Lee, Classification of pachychoroid disease on ultrawide-field indocyanine green angiography using auto-machine learning platform, British Journal of Ophthalmology 105 (6) (2021) 856–861. doi:10.1136/bjophthalmol-2020-316108.

[36] T. Ghosh, S. Tanwar, S. Chumber, K. Vani, Classification of chest radiographs using general purpose cloud-based automated machine learning: pilot study, Egyptian Journal of Radiology and Nuclear Medicine 52 (1) (2021) 1–9. doi:10.1186/s43055-021-00499-w.

[37] K. W. Wan, C. H. Wong, H. F. Ip, D. Fan, P. L. Yuen, H. Y. Fong, M. Ying, Evaluation of the performance of traditional machine learning algorithms, convolutional neural network and AutoML Vision in ultrasound breast lesions classification: a comparative study, Quantitative Imaging in Medicine and Surgery 11 (4) (2021) 1381. doi:10.21037/qims-20-922.

[38] A. Sakagianni, G. Feretzakis, D. Kalles, C. Koufopoulou, V. Kaldis, The Importance of Health Informatics in Public Health during a Pandemic, Vol. 272, IOS Press, 2020, Ch. Setting up an Easy-to-Use Machine Learning Pipeline for Medical Decision Support: A Case Study for COVID-19 Diagnosis Based on Deep Learning with CT Scans, p. 13–16. doi:10.3233/SHTI200481.

[39] Y. Zeng, J. Zhang, A machine learning model for detecting invasive ductal carcinoma with Google Cloud AutoML Vision, Computers in Biology and Medicine 122 (2020) 103861. doi:10.1016/j.compbiomed.2020.103861.

[40] A. A. Borkowski, C. P. Wilson, S. A. Borkowski, L. B. Thomas, L. A. Deland, S. J. Grewe, S. M. Mastorides, Comparing artificial intelligence platforms for histopathologic cancer diagnosis, Federal Practitioner 36 (10) (2019) 456.
URL https://www.ncbi.nlm.nih.gov/pmc/articles/PMC6837334/

[41] M. Puri, Automated machine learning diagnostic support system as a computational biomarker for detecting drug-induced liver injury patterns in whole slide liver pathology images, Assay and Drug Development Technologies 18 (1) (2020) 1–10. doi:10.1089/adt.2019.919.

[42] AutoGluon: AutoML for text, image, and tabular data (2021).

URL https://auto.gluon.ai/stable/index.html

[43] N. Erickson, J. Mueller, A. Shirkov, H. Zhang, P. Larroy, M. Li, A. Smola, AutoGluon-Tabular: Robust and accurate AutoML for structured data, arXiv:2003.06505 [stat.ML] (2020).
URL https://arxiv.org/abs/2003.06505

[44] N. Erickson, AutoGluon: Deep Learning AutoML, Medium towards data science (2019).
URL https://towardsdatascience.com/autogluon-deep-learning-automl-5cdb4e2388ec

[45] DATA Lab at Texas A&M University, AutoKeras (2021).
URL https://autokeras.com/

[46] H. Jin, Q. Song, X. Hu, Auto-keras: An efficient neural architecture search system, in: Proceedings of the 25th ACM SIGKDD International Conference on Knowledge Discovery & Data Mining, ACM, 2019, p. 1946–1956. doi:10.1145/3292500.3330648.

[47] A. Ye, AutoML: Creating top-performing neural networks without defining architectures (2020).
URL https://towardsdatascience.com/automl-creating-top-performing-neural-networks-without-defining-architectures-c7d3b08cddc

[48] AutoML Groups Freiburg and Hannover, Auto-PyTorch, GitHub (2021).
URL https://github.com/automl/Auto-PyTorch

[49] L. Zimmer, M. Lindauer, F. Hutter, Auto-Pytorch: Multi-fidelity metalearning for efficient and robust AutoDL, IEEE Transactions on Pattern Analysis and Machine Intelligence 43 (9) (2021). doi:10.1109/TPAMI.2021.3067763.

[50] google, google model_search, GitHub (2021).
URL https://github.com/google/model_search

[51] I. Belevich, E. Jokitalo, DeepMIB: User-friendly and open-source software for training of deep learning network for biological image segmentation, PLOS Computational Biology 17 (3) (2021) e1008374. doi:10.1371/journal.pcbi.1008374.

[52] Y. Wang, N. Coudray, Y. Zhao, F. Li, C. Hu, Y.-Z. Zhang, S. Imoto, A. Tsirigos, G. I. Webb, R. J. Daly, et al., HEAL: an automated deep learning framework for cancer histopathology image analysis, Bioinformatics (2021). doi:10.1093/bioinformatics/btab380.

[53] AutoGluon, PyPI (2021).
URL https://pypi.org/project/autogluon/

[54] N. Coudray, P. S. Ocampo, T. Sakellaropoulos, N. Narula, M. Snuderl, D. Fenyö, A. L. Moreira, N. Razavian, A. Tsirigos, Classification and mutation prediction from non–small cell lung cancer histopathology images using deep learning, Nature Medicine 24 (10) (2018) 1559. doi:10.1038/s41591-018-0177-5.

[55] J. N. Kather, A. T. Pearson, N. Halama, D. Jäger, J. Krause, S. H. Loosen, A. Marx, P. Boor, F. Tacke, U. P. Neumann, et al., Deep learning can predict microsatellite instability directly from histology in gastrointestinal cancer, Nature Medicine (2019) 1doi:10.1038/s41591-019-0462-y.

[56] E. Arvaniti, K. S. Fricker, M. Moret, N. Rupp, T. Hermanns, C. Fankhauser, N. Wey, P. J. Wild, J. H. Rueschoff, M. Claassen, Automated Gleason grading of prostate cancer tissue microarrays via deep learning, Scientific Reports 8 (1) (2018) 1–11. doi:10.1038/s41598-018-30535-1.

[57] S. Prasanna, Machine learning with AutoGluon, an open source AutoML library, AWS Open Source Blog (2020).
URL https://aws.amazon.com/blogs/opensource/machine-learning-with-autogluon-an-open-source-automl-library/

[58] NIH National Cancer Institute, The cancer genome atlas program (2021).
URL https://cancergenome.nih.gov/

[59] C. Szegedy, V. Vanhoucke, S. Ioffe, J. Shlens, Z. Wojna, Rethinking the inception architecture for computer vision, in: Proceedings of the IEEE Conference on Computer Vision and Pattern Recognition, 2016, p. 2818–2826. doi:10.1109/CVPR.2016.308.

[60] N. Coudray, DeepPATH, GitHub (2021).
URL https://github.com/ncoudray/DeepPATH

[61] J. N. Kather, Histological images for MSI vs. MSS classification in gastrointestinal cancer, FFPE samples, Zenodo (2019). doi:10.5281/zenodo.2530835.

[62] J. N. Kather, Histological images for MSI vs. MSS classification in gastrointestinal cancer, snap-frozen samples, Zenodo (2019). doi:10.5281/zenodo.2532612.

[63] J. N. Kather, MSIfromHE, GitHub (2019).
URL https://github.com/jnkather/MSIfromHE/

[64] K. He, X. Zhang, S. Ren, J. Sun, Deep residual learning for image recognition, in: Proceedings of the IEEE Conference on Computer Vision and Pattern Recognition, 2016, p. 770–778. doi:10.1109/CVPR.2016.90.

[65] E. Arvaniti, K. Fricker, M. Moret, N. Rupp, T. Hermanns, C. Fankhauser, N. Wey, P. Wild, J. H. Rüschoff, M. Claassen, Replication data for: Automated Gleason grading of prostate cancer tissue microarrays via deep learning, Harvard Dataverse (2018). doi:10.7910/DVN/OCYCMP.

[66] A. G. Howard, M. Zhu, B. Chen, D. Kalenichenko, W. Wang, T. Weyand, M. Andreetto, H. Adam, MobileNets: Efficient convolutional neural networks for mobile vision applications, arXiv:1704.04861 [cs.CV] (2017).
URL https://arxiv.org/abs/1704.04861

[67] D. Tellez, G. Litjens, P. Bándi, W. Bulten, J.-M. Bokhorst, F. Ciompi, J. van der Laak, Quantifying the effects of data augmentation and stain color normalization in convolutional neural networks for computational pathology, Medical Image Analysis 58 (2019) 101544. doi:10.1016/j.media.2019.101544.

[68] Genomic data commons data portal (2021).
URL https://portal.gdc.cancer.gov/

[69] Pillow, PyPI (2021).
URL https://pypi.org/project/Pillow/

[70] E. Arvaniti, eiriniar/gleason_cnn, GitHub (2019).
URL https://github.com/eiriniar/gleason_CNN

[71] ImageMagick Studio LLC, Imagemagick – convert, edit, or compose digital images (2021).
URL https://imagemagick.org/

[72] NumPY, PyPI (2021).
URL https://pypi.org/project/numpy/

[73] A. Buslaev, V. I. Iglovikov, E. Khvedchenya, A. Parinov, M. Druzhinin, A. A. Kalinin, Albumentations: fast and flexible image augmentations, Information 11 (2) (2020) 125. doi:10.3390/info11020125.

[74] albumentations, PyPI (2021).
URL https://pypi.org/project/albumentations/

[75] F. Pedregosa, G. Varoquaux, A. Gramfort, V. Michel, B. Thirion, O. Grisel, M. Blondel, P. Prettenhofer, R. Weiss, V. Dubourg, V. Dubourg, J. Vanderplas, A. Passos, D. Cournapeau, M. Brucher, M. Perrot, É. Duchesnay, Scikit-learn: Machine learning in Python, Journal of Machine Learning Research 12 (Oct) (2011) 2825–2830, arXiv:1201.0490v3 [cs.LG].
URL https://arxiv.org/abs/1201.0490

[76] scikit-learn, PyPi (2021).
URL https://pypi.org/project/scikit-learn/

[77] D. Nüst, V. Sochat, B. Marwick, S. J. Eglen, T. Head, T. Hirst, Ten simple rules for writing dockerfiles for reproducible data science, PLOS Comptational Biology 16 (11) (2020) e1008316. doi:10.1371/journal.pcbi.1008316.

[78] L. Li, A. Talwalkar, Random search and reproducibility for neural architecture search, in: Proceedings of The 35th Uncertainty in Artificial Intelligence Conference PMLR 2020, PMLR, 2020, p. 367–377.
URL https://proceedings.mlr.press/v115/li20c.html

[79] M. Lindauer, F. Hutter, Best practices for scientific research on neural architecture search, Journal of Machine Learning Research 21 (243) (2020) 1–18.
URL https://www.jmlr.org/papers/volume21/20-056/20-056.pdf

[80] J. Deng, W. Dong, R. Socher, L.-J. Li, K. Li, L. Fei-Fei, ImageNet: A large-scale hierarchical image database, in: 2009 IEEE Conference on Computer Vision and Pattern Recognition, 2009, p. 248–255. doi:10.1109/CVPR.2009.5206848.

[81] M. Tan, B. Chen, R. Pang, V. Vasudevan, M. Sandler, A. Howard, Q. V. Le, MnasNet: Platform-aware neural architecture search for mobile, in: Proceedings of the IEEE/CVF Conference on Computer Vision and Pattern Recognition, 2019, p. 2820–2828. doi:10.1109/CVPR.2019.00293.

[82] AutoMLEvalComputationalPathology (2021).
URL https://gitlab.com/oschwen/AutoMLEvalComputationalPathology

[83] G. Piantadosi, S. Marrone, C. Sansone, On reproducibility of deep convolutional neural networks approaches, in: International Workshop on Reproducible Research in Pattern Recognition, Vol. 11455 of Lecture Notes in Computer Science, 2018, p. 104–109. doi:10.1007/978-3-030-23987-9_10.

[84] S. Marrone, S. Olivieri, G. Piantadosi, C. Sansone, Reproducibility of deep CNN for biomedical image processing across frameworks and architectures, in: 2019 27th European Signal Processing Conference (EUSIPCO), IEEE, 2019, p. 1–5. doi:10.23919/EUSIPCO.2019.8902690.

[85] H.-G. Nguyen, A. Blank, H. E. Dawson, A. Lugli, I. Zlobec, Classification of colorectal tissue images from high throughput tissue microarrays by ensemble deep learning methods, Scientific Reports 11 (1) (2021) 1–11. doi:10.1038/s41598-021-81352-y.

[86] T. Lindsey, J.-J. Lee, Automated cardiovascular pathology assessment using semantic segmentation and ensemble learning, Journal of Digital Imaging (2020) 1–6doi:10.1007/s10278-019-00197-0.

[87] S. H. Kassani, P. H. Kassani, M. J. Wesolowski, K. A. Schneider, R. Deters, Classification of histopathological biopsy images using ensemble of deep learning networks, in: Proceedings of the 29th Annual International Conference on Computer Science and Software Engineering, 2019, p. 92–99.
URL https://arxiv.org/abs/1909.11870

[88] S. Qummar, F. G. Khan, S. Shah, A. Khan, S. Shamshirband, Z. U. Rehman, I. A. Khan, W. Jadoon, A deep learning ensemble approach for diabetic retinopathy detection, IEEE Access 7 (2019) 150530–150539. doi:10.1109/ACCESS.2019.2947484.

[89] M. A. Ganaie, M. Hu, et al., Ensemble deep learning: A review, arXiv:2104.02395 [cs.LG] (2021).
URL https://arxiv.org/abs/2104.02395

[90] A. Echle, N. T. Rindtorff, T. J. Brinker, T. Luedde, A. T. Pearson, J. N. Kather, Deep learning in cancer pathology: a new generation of clinical biomarkers, British Journal of Cancer (2020) 1–11doi:10.1038/s41416-020-01122-x.

[91] F. Isensee, P. F. Jaeger, S. A. A. Kohl, J. Petersen, K. H. Maier-Hein, nnU-Net: a self-configuring method for deep learning-based biomedical image segmentation, Nature Methods (2020) 1–9doi:10.1038/s41592-020-01008-z.

[92] M. Baumgartner, P. F. Jaeger, F. Isensee, K. H. Maier-Hein, nnDetection: A self-configuring method for medical object detection, arXiv:2106.00817 [cs.CV] (2021).
URL https://arxiv.org/abs/2106.00817

[93] M. Raghu, C. Zhang, J. Kleinberg, S. Bengio, Transfusion: Understanding transfer learning for medical imaging, in: Proceedings of the 33rd International Conference on Neural Information Processing Systems NIPS'19, no. 301, 2019, p. 3347–3357.
URL https://dl.acm.org/doi/abs/10.5555/3454287.3454588

[94] S. Wang, D. M. Yang, R. Rong, X. Zhan, G. Xiao, Pathology image analysis using segmentation deep learning algorithms (2019). doi:10.1016/j.ajpath.2019.05.007.

[95] D. Tellez, G. Litjens, J. van der Laak, F. Ciompi, Neural image compression for gigapixel histopathology image analysis, IEEE Transactions on Pattern Analysis and Machine Intelligence (2019). doi:10.1109/TPAMI.2019.2936841.

[96] D. Tellez, D. Höppener, C. Verhoef, D. Grünhagen, P. Nierop, M. Drozdzal, J. Laak, F. Ciompi, Extending unsupervised neural image compression with supervised multitask learning, in: Medical Imaging with Deep Learning, PMLR, 2020, p. 770–783.
URL https://proceedings.mlr.press/v121/tellez20a/tellez20a.pdf

[97] M. Y. Lu, D. Kong, J. Lipkova, R. J. Chen, R. Singh, D. F. K. Williamsona, T. Y. Chena, F. Mahmood, Federated learning for computational pathology on gigapixel whole slide images, arXiv:2009.10190 [eees.IV] (2020).
URL https://arxiv.org/abs/2009.10190

[98] M. J. Sheller, B. Edwards, G. A. Reina, J. Martin, S. Pati, A. Kotrotsou, M. Milchenko, W. Xu, D. Marcus, R. R. Colen, et al., Federated learning in medicine: facilitating multi-institutional collaborations without sharing patient data, Scientific Reports 10 (12598) (2020) 1–12.

doi:10.1038/s41598-020-69250-1.

[99] I. Dayan, H. R. Roth, A. Zhong, A. Harouni, A. Gentili, A. Z. Abidin, A. Liu, A. B. Costa, B. J. Wood, C.-S. Tsai, et al., Federated learning for predicting clinical outcomes in patients with COVID-19, Nature Medicine (2021) 1–9doi:10.1038/s41591-021-01506-3.

[100] J. M. Johnson, T. M. Khoshgoftaar, Survey on deep learning with class imbalance, Journal of Big Data 6 (1) (2019) 1–54. doi:10.1186/s40537-019-0192-5.

[101] A. Bria, C. Marrocco, F. Tortorella, Addressing class imbalance in deep learning for small lesion detection on medical images, Computers in Biology and Medicine 120 (2020) 103735. doi:10.1016/j.compbiomed.2020.103735.

[102] K. Stacke, G. Eilertsen, J. Unger, C. Lundström, A closer look at domain shift for deep learning in histopathology, MICCAI 2019 Workshop COMPAY (2019).
URL https://openreview.net/forum?id=rkeVzGaobS

[103] B. E. Bejnordi, G. Litjens, N. Timofeeva, I. Otte-Höller, A. Homeyer, N. Karssemeijer, J. A. W. M. van der Laak, Stain specific standardization of whole-slide histopathological images, IEEE Transactions on Medical Imaging 35 (2) (2016) 404–415. doi:10.1109/TMI.2015.2476509.

[104] D. Bug, S. Schneider, A. Grote, E. Oswald, F. Feuerhake, J. Schüler, D. Merhof, Deep Learning in Medical Image Analysis and Multimodal Learning for Clinical Decision Support, Vol. 10553 of Lecture Notes in Computer Science, Springer, 2017, Ch. Context-based normalization of histological stains using deep convolutional features, p. 135–142. doi:10.1007/978-3-319-67558-9_16.

[105] T. Kalinski, R. Zwönitzer, F. Grabellus, S.-Y. Sheu, S. Sel, H. Hofmann, A. Roessner, Lossless compression of JPEG2000 whole slide images is not required for diagnostic virtual microscopy, American Journal of Clinical Pathology 136 (6) (2011) 889–895. doi:10.1309/AJCPYI1Z3TGGAIEP.

[106] G. Mariani, F. Scheidegger, R. Istrate, C. Bekas, C. Malossi, BAGAN: Data augmentation with balancing GAN, arXiv:1803.09655 [cs.CV] (2018).
URL https://arxiv.org/abs/1803.09655

[107] G. Huang, A. H. Jafari, Enhanced balancing GAN: Minority-class image generation, Neural Computing and Applications (2021) 1–10doi:10.1007/s00521-021-06163-8.

Appendix A. Code

The code for preprocessing data, running AutoGluon to generate CNNs (AutoGluon only), and evaluating the resulting classifiers (AutoGluon and AutoML Vision) is available from [82].

Appendix B. Details on datasets

The splitting strategies following the original publications (described in the Methods section) resulted in the sizes of splits shown in Tables B.3, B.4, and and B.5 as well as the class balances shown in Tables B.6, B.7, and B.8.

Appendix C. Hyperparameter optimization

Training parameters and accuracies during hyperparameter optimization are shown in Figure C.3 (tissue classification), Figure C.4 (mutation prediction), and Figure C.5 (grading use case). These accuracies are tile-based accuracies and thus lower than the metrics used for classifier performance (slide-based ROC-AUC and tile-based quadratically weighted Cohen's κ)

Table B.3: Tile statistics, tissue classification use case. These datasets were split at the patient level (indicated by *) For use with AutoML Vision, the datasets needed to be limited to 1 million images. As the subsequent evaluation was run separately and not subject to this limit, the LUAD vs. LUSC task used the full training and validation sets, the other two tasks used 820850 training and 179050 validation tiles.

	Tiles			Slides			Patients*		
Task	Training	Validation	Test	Training	Validation	Test	Training*	Validation*	Test*
normal vs. tumor normal vs. LUAD vs. LUSC	926335 (70%)	202059 (15%)	200799 (15%)	1473 (68%)	350 (16%)	344 (16%)	739 (73%)	143 (14%)	127 (13%)
LUAD vs LUSC	756378 (70%)	162625 (15%)	162678 (15%)	1084 (69%)	249 (16%)	243 (15%)	719 (72%)	141 (14%)	134 (13%)

Table B.4: Tile statistics, mutation prediction use case. The test set was split at the patient level, whereas training and validation data were split at the tile level (indicated by *)

	Tiles*			Slides			Patients*		
Task (Dataset)	Training*	Validation*	Test	Training	Validation	Test	Training	Validation	Test*
CRC_DX	79397 (42%)	11676 (6%)	98904 (52%)	263 (42%)	262 (42%)	101 (16%)	260 (42%)	259 (42%)	100 (16%)
CRC_KR	51760 (38%)	7612 (6%)	78249 (57%)	504 (42%)	484 (41%)	199 (17%)	278 (42%)	271 (41%)	109 (17%)
STAD	85484 (40%)	12572 (6%)	118008 (55%)	199 (40%)	198 (40%)	103 (21%)	185 (40%)	184 (39%)	99 (21%)

Table B.5: Tile statistics, Grading use case. This dataset was split at the TMA level (indicated by *). Training data was subsequently oversampled 8-fold, effectively resulting in 201696 image tiles. The test data in this use case was assessed separately by two observers.

	Tiles			Tissue Microarrays*			Patients		
	Training	Validation	Test	Training*	Validation*	Test*	Training	Validation	Test
TMA dataset	25212 (79%)	2482 (8%)	4237 (13%)	3 (60%)	1 (20%)	1 (20%)	508	133	245

Table B.6: Class statistics (number of tiles), tissue classification use case

	Normal vs. tumor		LUAD vs. LUSC	
	Normal	Tumor	LUAD	LUSC
Training tiles	164119 (18%)	762216 (82%)	369683 (49%)	386695 (51%)
Validation tiles	37883 (19%)	164176 (81%)	79691 (49%)	82934 (51%)
Test tiles	45510 (23%)	155289 (77%)	79625 (49%)	83053 (51%)

	normal vs. LUAD vs. LUSC		
	Normal	LUAD	LUSC
Training tiles	164119 (18%)	372021 (40%)	390195 (42%)
Validation tiles	37883 (19%)	80724 (40%)	83452 (41%)
Test tiles	45510 (23%)	76254 (38%)	79035 (39%)

Table B.7: Class statistics (number of tiles), mutation prediction use case.

Datset	Split set	MSS	MSI
CRC_DX	Training	39705 (50%)	39692 (50%)
	Validation	5839 (50%)	5837 (50%)
	Test	70569 (71%)	28335 (29%)
CRC_KR	Training	25906 (50%)	25854 (50%)
	Validation	3780 (50%)	3832 (50%)
	Test	60574 (77%)	17675 (23%)
STAD	Training	42729 (50%)	42755 (50%)
	Validation	6303 (50%)	6269 (50%)
	Test	90104 (76%)	27904 (24%)

Table B.8: Class statistics (number of tiles), grading use case.

	0	3	4	5
Training	2076 (14%)	6303 (41%)	4541 (30%)	2383 (16%)
Training, augmented	50424	50424	50424	50424
augmentation/oversampling factor	24.3-fold	8-fold	11.1-fold	21.2-fold
Validation	666 (27%)	923 (37%)	573 (23%)	320 (13%)
Test (pathologist 1)	127 (3%)	1602 (38%)	2121 (50%)	387 (9%)
Test (pathologist 2)	90 (2%)	861 (20%)	2715 (64%)	571 (13%)

Interestingly, validation accuracies for the mutation prediction use case (Figure C.4) are consistently higher than the training accuracies. This is the only use case where training and validation data overlap in patients, but otherwise the reasons for this effect are unclear.

Appendix D. Details on reproducibility

We computed variabilities of metrics of intermediate steps when aggregating tile-based classification results to slide-based classification for a more detailed analysis: For the tile-based classification, i.e., the immediate output of the CNNs, we computed means, standard deviations, and coefficients of variation of the confusion matrices over the seven repeated experiments. Moreover, we computed means, standard deviations, and coefficients of variation of the tile-based accuracy and AUROC in addition to the slide-based AUROC (tissue classification use case, Tables D.9 and D.10; mutation prediction use case, Tables D.11 and D.12) as well as for the tile-based quadratically weighted Cohen's κ (grading use case, Tables D.13 and D.14).

Appendix E. Bootstrapped confidence intervals

In [54], the authors computed 95% confidence intervals estimating how well the trained CNNs would generalize beyond the available data by 1000-fold bootstrapping of the per-slide predictions, resulting in ranges of (0.974, 1.000) for normal vs. tumor, (0.913, 0.980) for LUSC vs. LUAD, and (0.947, 1.000)/(0.933, 0.994)/(0.935, 0.990) for normal vs. rest/LUAD vs. rest/LUSC vs. rest. In [55], the authors used the same approach as in [54] to compute 95% confidence intervals by 2000-fold bootstrapping over the test data, resulting in (0.72, 0.92) for CRC-DX, (0.62, 0.87) for CRC-KR, and (0.69, 0.90) for STAD. No such confidence intervals are reported for the tile classification in [56]. We used the same approach with 2000-fold bootstrapping to obtain confidence intervals for all three use cases, shown in Figure E.6.

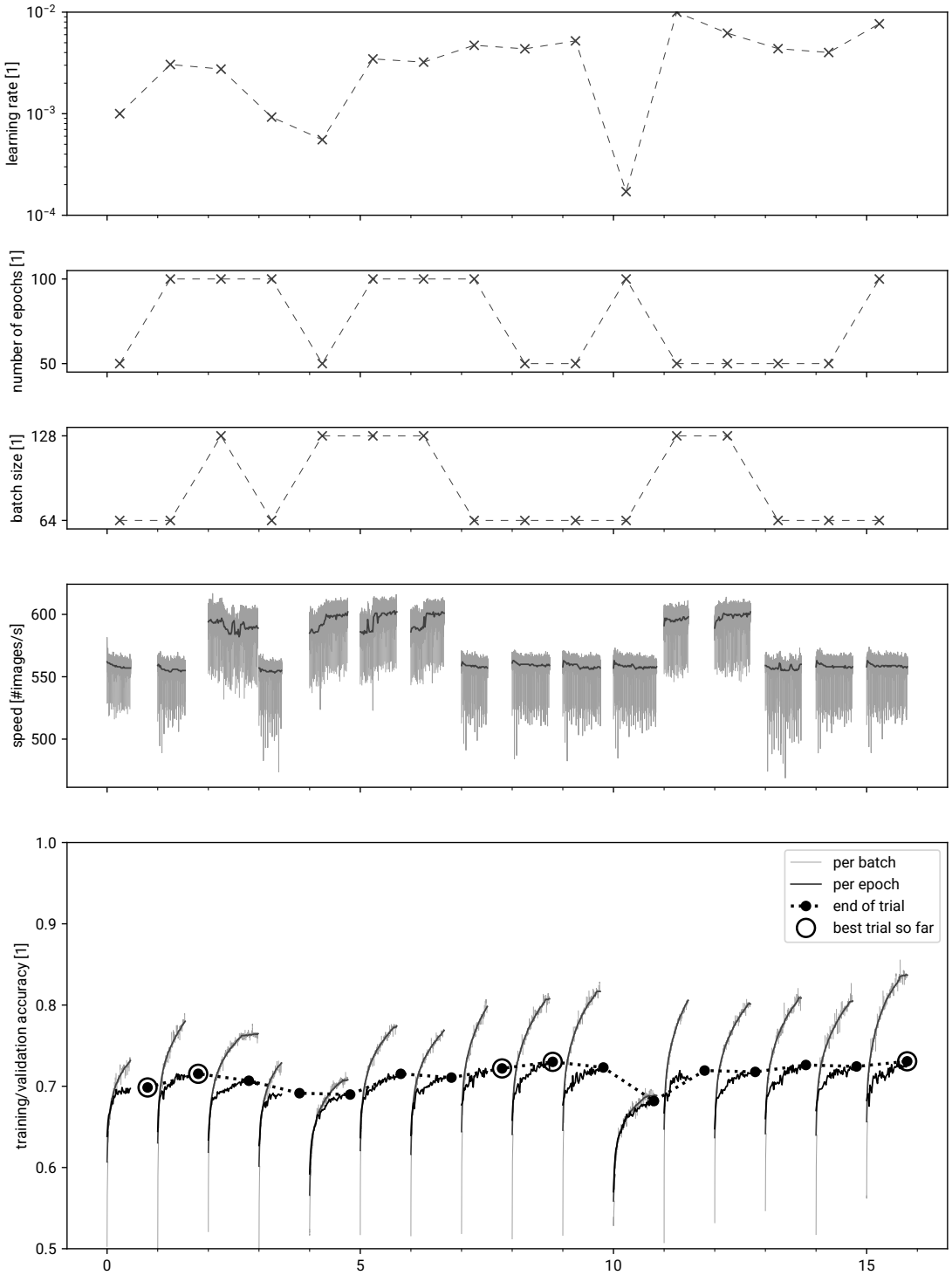

Figure C.3: Training parameters and accuracies during hyperparameter optimization, tissue classification use case. Thin lines: training data, thick lines: validation data.

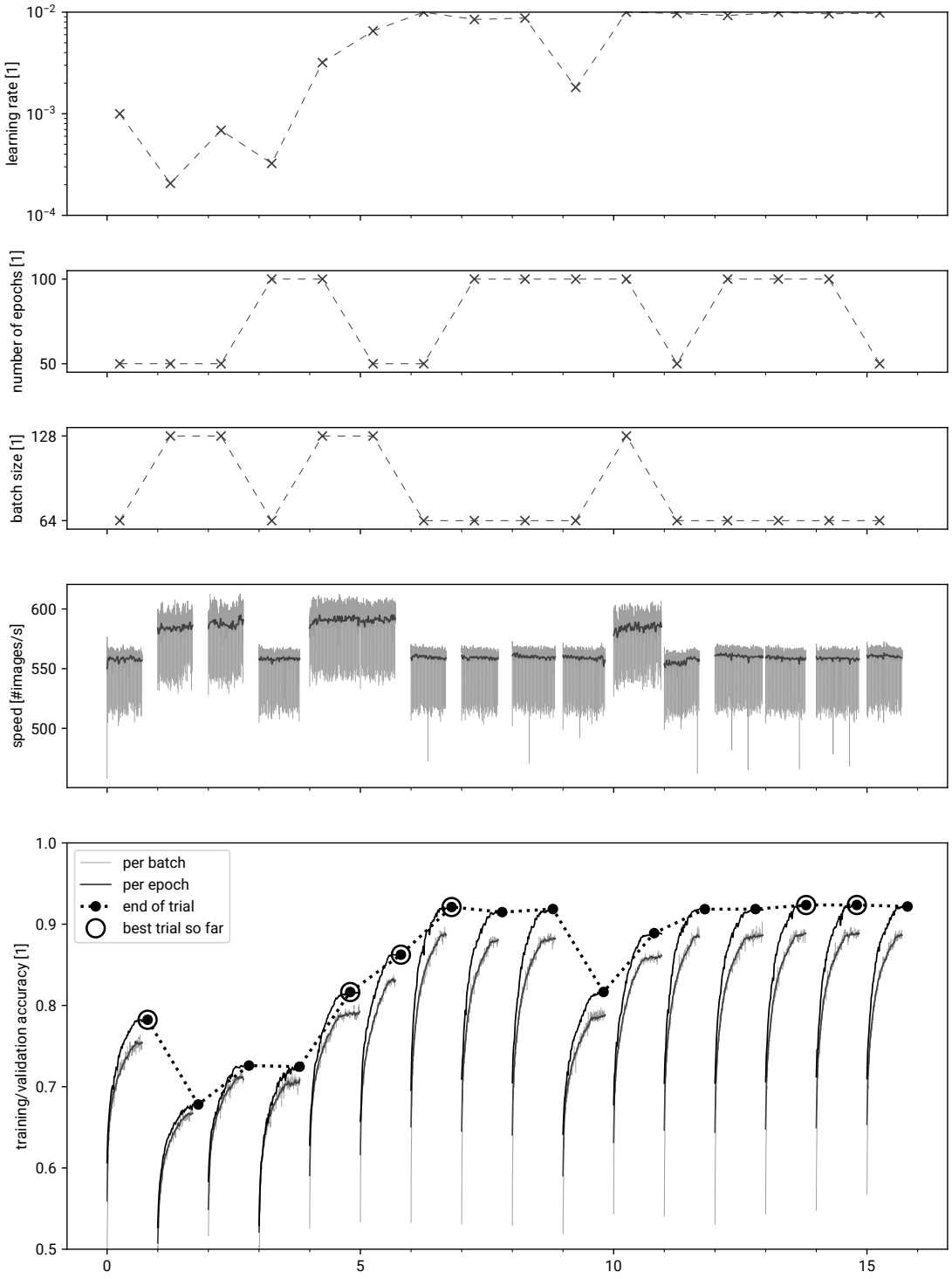

Figure C.4: Training parameters and accuracies during hyperparameter optimization, mutation prediction use case. Thin lines: training data, thick lines: validation data.

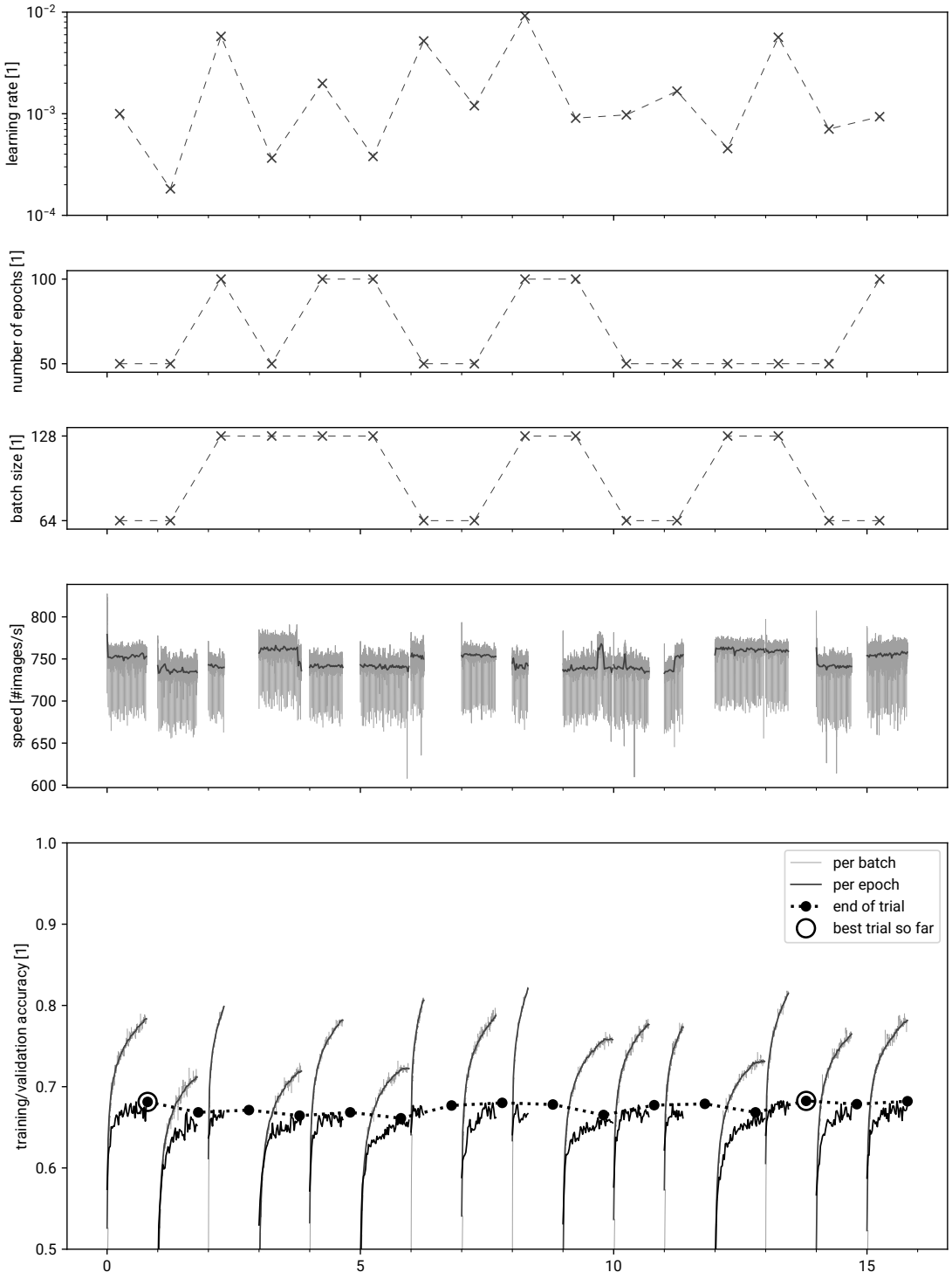

Figure C.5: Training parameters and accuracies during hyperparameter optimization, grading use case. Thin lines: training data, thick lines: validation data.

Table D.9: Variability of the confusion matrix (column: actual class, row: predicted class) of tile predictions, mean ± standard deviation (coefficient of variation in percent) over seven experiments for the tissue classification use case.

AutoGluon	LUAD	LUSC
LUAD	61155.6 ± 1296.4 (2.1%)	18469.4 ± 1296.4 (7.0%)
LUSC	25368.1 ± 1093.6 (4.3%)	57684.9 ± 1093.6 (1.9%)
AutoML Vision	**LUAD**	**LUSC**
LUAD	58642.0 ± 1484.4 (2.5%)	20983.0 ± 1484.4 (7.1%)
LUSC	19541.9 ± 2122.5 (10.9%)	63511.1 ± 2122.5 (3.3%)

Table D.10: Variability of aggregated metrics for the tissue classification use case.

	AutoGluon	AutoML Vision
Accuracy tile-based	0.731 ± 0.0060 (0.8%)	0.750 ± 0.0125 (1.7%)
AUROC tile-based	0.812 ± 0.0065 (0.8%)	0.830 ± 0.0133 (1.6%)
AUROC slide-based	0.930 ± 0.0027 (0.3%)	0.937 ± 0.0072 (0.8%)

Table D.11: Variability of the confusion matrix (column: actual class, row: predicted class) of tile predictions, mean ± standard deviation (coefficient of variation in percent) over seven experiments for the mutation prediction use case.

AutoGluon	MSI	MSS
MSI	13316.9 ± 405.1 (3.0%)	14587.1 ± 405.1 (2.8%)
MSS	17755.6 ± 769.8 (4.3%)	72348.4 ± 769.8 (1.1%)
AutoML Vision	**MSI**	**MSS**
MSI	7884.0 ± 359.1 (4.6%)	20020.0 ± 359.1 (1.8%)
MSS	10026.1 ± 618.0 (6.2%)	80077.9 ± 618.0 (0.8%)

Table D.12: Variability of aggregated metrics for the mutation prediction use case.

	AutoGluon	AutoML Vision
Accuracy tile-based	0.726 ± 0.0034 (0.5%)	0.747 ± 0.0037 (0.5%)
ROC-AUC tile-based	0.709 ± 0.0017 (0.2%)	0.651 ± 0.0121 (1.9%)
ROC-AUC slide-based	0.792 ± 0.0027 (0.3%)	0.755 ± 0.0158 (2.1%)

Table D.13: Variability of the confusion matrix (column: actual class, row: predicted class) of tile predictions, mean ± standard deviation (coefficient of variation in percent) over seven experiments for the grading use case.

AutoGluon	Test vs. P1			
	0	3	4	5
0	67.7 ± 5.9 (8.7%)	47.7 ± 7.1 (14.8%)	9.6 ± 2.2 (22.9%)	2.0 ± 1.1 (53.5%)
3	27.1 ± 5.1 (18.7%)	1095.9 ± 47.2 (4.3%)	459.6 ± 50.1 (10.9%)	19.4 ± 6.2 (31.9%)
4	28.6 ± 10.1 (35.4%)	441.1 ± 58.0 (13.2%)	1443.7 ± 73.0 (5.1%)	207.6 ± 34.9 (16.8%)
5	6.4 ± 2.1 (32.0%)	18.1 ± 3.9 (21.7%)	165.9 ± 18.2 (10.9%)	196.6 ± 17.7 (9.0%)
	Test vs. P2			
	0	3	4	5
0	57.3 ± 3.0 (5.2%)	24.9 ± 4.2 (17.0%)	6.7 ± 1.5 (22.1%)	1.1 ± 0.8 (72.9%)
3	27.1 ± 4.6 (17.6%)	647.0 ± 19.1 (3.0%)	181.7 ± 20.4 (11.2%)	5.1 ± 2.9 (57.3%)
4	35.3 ± 11.7 (33.1%)	876.3 ± 79.0 (9.0%)	1580.1 ± 94.1 (6.0%)	223.3 ± 37.2 (16.7%)
5	10.1 ± 3.6 (35.5%)	54.7 ± 11.6 (21.1%)	310.1 ± 21.4 (6.9%)	196.0 ± 18.5 (9.4%)
AutoML Vision	Test vs. P1			
	0	3	4	5
0	185.0±77.2 (41.7%)	52.0±47.0 (90.5%)	137.0±54.1 (39.5%)	13.0±6.4 (49.5%)
3	0.3±0.5 (170.8%)	107.0±10.7 (10.0%)	2.1±2.3 (109.2%)	17.6±10.0 (57.1%)
4	231.0±141.6 (61.3%)	185.3±106.8 (57.6%)	1279.6±218.6 (17.1%)	425.1±237.8 (55.9%)
5	22.6±16.8 (74.5%)	186.1±75.2 (40.4%)	367.4±154.6 (42.1%)	1025.9±168.6 (16.4%)
	Test vs. P2			
	0	3	4	5
0	197.4±83.0 (42.0%)	57.4±47.3 (82.4%)	277.6±63.1 (22.7%)	38.6±22.7 (58.9%)
3	0.3±0.5 (170.8%)	79.0±5.1 (6.5%)	1.9±2.0 (109.6%)	8.9±4.3 (49.0%)
4	236.1±150.3 (63.6%)	252.4±136.0 (53.9%)	1369.7±292.8 (21.4%)	856.7±311.8 (36.4%)
5	5.0±5.2 (103.9%)	141.6±48.5 (34.3%)	137.0±64.1 (46.8%)	577.4±81.3 (14.1%)

Table D.14: Variability of the aggregated metric, quadratically weighted Cohen's κ, for the grading use case.

	AutoGluon		AutoML Vision	
	Test vs. P1	Test vs. P2	Test vs. P1	Test vs. P2
κ	0.573 ± 0.0034 (0.6%)	0.465 ± 0.0129 (2.8%)	0.469 ± 0.117 (24.8%)	0.384 ± 0.101 (26.3%)

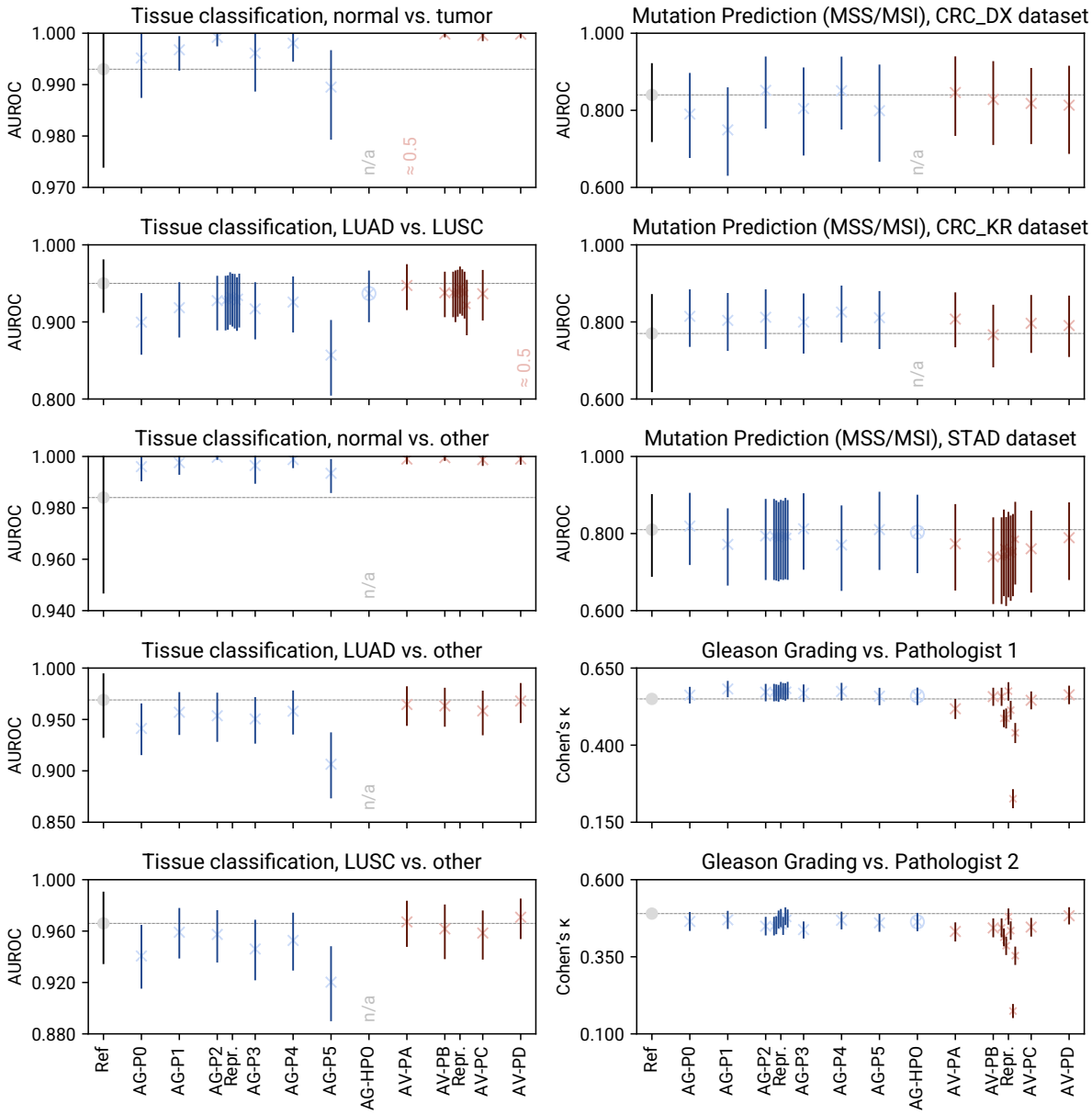

Figure E.6: 95% confidence intervals obtained by 2000-fold bootstrapping over the per-slide predictions (tissue classification and mutation prediction use cases) and per-tile predictions (grading use case)